








RESEARCH ARTICLE | OCTOBER 19 2021

Proton irradiation induced chemical ordering in an $\text{Al}_{0.3}\text{CoFeNi}$ high entropy alloy **FREE**

Special Collection: [Metastable High Entropy Alloys](#)Sriswaroop Dasari ; Abhishek Sharma ; Todd A. Byers ; Gary A. Glass; Srinivasan Srivilliputhur ; Bibhudutta Rout ; Rajarshi Banerjee  *Appl. Phys. Lett.* 119, 161907 (2021)<https://doi.org/10.1063/5.0065875>

CrossMark



APL Quantum

Bridging fundamental quantum research with technological applications

Now Open for Submissions

No Article Processing Charges (APCs) through 2024

Submit Today

 AIP
Publishing

Proton irradiation induced chemical ordering in an $\text{Al}_{0.3}\text{CoFeNi}$ high entropy alloy

Cite as: Appl. Phys. Lett. **119**, 161907 (2021); doi: [10.1063/5.0065875](https://doi.org/10.1063/5.0065875)

Submitted: 5 August 2021 · Accepted: 7 October 2021 ·

Published Online: 19 October 2021



View Online



Export Citation



CrossMark

Sriswaroop Dasari,¹  Abhishek Sharma,¹  Todd A. Byers,²  Gary A. Glass,² Srinivasan Srivilliputhur,¹  Bibhudutta Rout,²  and Rajarshi Banerjee^{1,a)} 

AFFILIATIONS

¹Department of Materials Science and Engineering, University of North Texas, Denton, Texas 76207, USA

²Department of Physics, University of North Texas, Denton, Texas 76203, USA

Note: This paper is part of the APL Special Collection on Metastable High Entropy Alloys.

^{a)} Author to whom correspondence should be addressed: raj.banerjee@unt.edu

ABSTRACT

The radiation resistance of single-phase high entropy alloys has been reported to be superior to conventional alloys, due to their high lattice distortion and sluggish diffusion kinetics. The current study combines the beneficial effects of a concentrated multi-component solid solution and chemical ordering on the parent lattice of a candidate alloy, $\text{Al}_{0.3}\text{CoFeNi}$, to enhance proton radiation resistance. The strong ordering tendency in this alloy results in the formation of Ni-Al-rich short-range ordered (SRO) domains when it is annealed in a single FCC phase field and water quenched. The irradiation of these microstructures with high-fluence MeV-energetic protons aids the transformation of the prior metastable single FCC solid-solution with SRO domains toward a more stable condition with L_{12} long-range ordered (LRO) domains embedded within the FCC solid solution matrix. Potentially, the creation of radiation-induced vacancy cascades within the FCC solid-solution enhances local diffusivity aiding the transition from SRO domains to LRO L_{12} domains. Therefore, this can be considered as a recovery mechanism, since the radiation-induced damage is not allowed to accumulate and is minimized via nanometer-scale precipitation of the ordered intermetallic phase. Additionally, preferential Co segregation to defect clusters or dislocation loops was also observed. In comparison, purely thermal activation via annealing at 500 °C for 30 min induces a similar transformation from SRO to LRO in this alloy, driving the system closer to equilibrium.

Published under an exclusive license by AIP Publishing. <https://doi.org/10.1063/5.0065875>

High entropy alloys (HEAs) or complex concentrated alloys (CCAs) have shown potential for structural applications due to their promising mechanical properties, corrosion, and wear resistance.^{1–4} Recently, the core effects, especially lattice distortion and sluggish diffusion, proposed in HEAs attracted research into irradiation resistance as well.^{5–8} However, it must be noted that the existence of the above-mentioned core effects in HEAs is still under debate.^{9–15} Nevertheless, this new class of alloys has been shown to exhibit good irradiation resistance compared to conventional alloys. In particular, FCC-based HEAs in the Co-Cr-Fe-Mn-Ni alloy system have received much attention to understand the role of multiple components on irradiation resistance.^{6,16–18} High local stresses at the atomic scale leading to amorphization followed by recrystallization^{7,8} and sluggish diffusion kinetics of radiation-induced defects^{6,16} were proposed as the mechanisms behind enhanced irradiation resistance of HEAs.

A systematic investigation on the effect of compositional complexity on irradiation resistance was carried out by Lu *et al.*¹⁶ It was

observed that with the increasing number of elements in the Co-Cr-Fe-Mn-Ni alloy system, the growth of dislocation loops is inhibited and radiation-induced segregation (RIS) is suppressed. Additionally, molecular static simulations indicated that a disk-like segregation is preferred around the faulted dislocation loops instead of the ring shape. RIS of alloying elements to defects such as dislocation loops and grain boundaries is an important phenomenon that severely impacts the material performance during or post-irradiation. Preferential Co and Ni segregation to dislocation loops at high temperature through vacancy flux has been reported by Chen *et al.*¹⁹ Barr *et al.*¹⁷ reported Co and Ni enrichment and depletion of Mn at the grain boundaries after irradiating CoCrFeMnNi with 3 MeV Ni ions. In a study by Jin *et al.*,¹⁸ Fe and Mn were found to be the most beneficial elements in suppressing swelling from irradiation. Thus, the irradiation studies on FCC-based HEAs have so far been focused on single-phase solid solutions. However, multi-phase alloys provide a good opportunity to obtain better mechanical performance, especially

at high temperatures. Therefore, investigating the irradiation resistance of multi-phase alloys becomes imperative in developing high-temperature radiation-resistant materials. The reports on the irradiation resistance of multi-phase HEAs are rather limited. Nagase *et al.*⁷ compared the effects of irradiation with annealing of CoCrCuFeNi alloy and observed that both induce similar phase changes. The formation of ordered intermetallic compounds has also been reported in this study, but their phase fraction was very low. The irradiation behavior of multi-phase microstructures in $\text{Al}_x\text{CoCrFeNi}$ system has been investigated by Xia *et al.*²⁰ It was observed that as the Al content (x) is increased from 0.1 to 0.75 to 1.5, the microstructure was transitioned from FCC to FCC+BCC to BCC, with a corresponding increase in radiation-induced swelling. Kombaiah *et al.*²¹ reported the formation of L_{12} phase in FCC matrix of $\text{Al}_{0.12}\text{CoCrFeNi}$, when the alloy was irradiated using Ni^{2+} ions at a temperature of 500 °C. The post-irradiation microstructure was characterized using transmission electron microscopy, which revealed precipitation of L_{12} phase. TEM analysis of unirradiated alloy annealed at 500 °C for 490 h, however, did not reveal any L_{12} precipitation, suggesting that L_{12} may not be an equilibrium phase in this alloy at 500 °C.

In the present work, the base alloy CoFeNi was chosen because it was reported previously²² that this ternary combination leads to a near-randomness distribution of elements. This combination of elements was also reported to possess very high swelling resistance among the six Ni-containing solid solution alloys in the Co-Cr-Fe-Mn-Ni system.¹⁸ The advantages offered by CoFeNi were further coupled with an ordering tendency that can be introduced by Al addition. The effects of proton irradiation on $\text{Al}_{0.3}\text{CoFeNi}$ multi-component alloy on ordering and radiation-induced segregation have been investigated in this study. Furthermore, these results were compared with thermally induced microstructural changes via annealing of the same alloy. However, it must be noted that the current investigation is focused on the effects of proton irradiation performed at room temperature on HEAs with ordering tendency. The created damages can be comparable to neutron induced damages.²³ Potential applications for these alloys include light water reactor cores,²³ reactor pressure vessels,²⁴ and accident tolerance fuel (ATF) cladding.²⁵ The microstructure of post-irradiated alloy was characterized using complementary advanced microscopy techniques, i.e., transmission electron microscopy (TEM) and atom probe tomography (APT). Such coupling of techniques has resulted in identifying the size, distribution, and composition of the ordered domains that formed up on irradiation at room temperature. These parameters are important in correlating the amount of irradiation with the mechanical properties of the irradiated layer, which is a subject of future study.

A high entropy alloy with a nominal chemical composition $\text{Al}_{0.3}\text{CoFeNi}$ (8.2Al-30.6Co-30.6Fe-30.6Ni in at. %) was prepared in a conventional vacuum arc melter. The cast ingot was homogenized at 1200 °C for 1-h and then cold rolled to 90% reduction in thickness. The cold-rolled alloy was subjected to a solution annealing treatment at 1200 °C for 5 min, water quenched. All specimens were encapsulated in quartz tubes backfilled with argon for heat treatments and water quenched. Thereafter, the samples were irradiated using 1.4 MeV protons with two fluences 0.8×10^{18} ions/cm² and 2.33×10^{18} ions/cm² from a 3 MV Pelletron accelerator (NEC-9SH).²⁶ The beams were raster-scanned at a target area of 1.5×0.5 cm² with a beam flux of 3.33×10^{13} ions/cm²s, and the target temperature was periodically measured using an IR camera and increased to 80 °C.

Microstructural characterization was done using TEM (FEI Tecnai G2 TF20TM operating at 200 kV and JEOL JEM-3000F HRTEM operating at 300 kV) to obtain crystallographic information from the phases present in the material. APT was performed using Cameca LEAP 5000XS 3D Atom Probe Microscope operating at a temperature of 30 K, pulse rate of 200 kHz, and a detection rate of 0.005–0.01 ion/pulse in laser mode with a laser pulse energy of 50 nJ. The samples for TEM and APT were prepared using the site-specific lift-out technique on a FEITM Nova 200 dual-beam focused ion beam (FIB).

The results from the microstructural characterization of the $\text{Al}_{0.3}\text{CoFeNi}$ alloy in the solutionized and quenched conditions are given in the [supplementary material](#), Fig. S1. While the TEM results confirm the presence of a single FCC phase, APT results indicate the presence of compositionally clustered Ni-Al-rich domains. These Ni-Al-rich clusters are ~ 2.5 nm in size and contain ~ 32 at. % Ni and 12 at. % Al, as opposed to 28 at. % Ni and ~ 7.5 at. % Al in the parent matrix. Based on thermodynamic considerations, this preferential pairing of unlike elements, with a negative enthalpy of mixing (Ni and Al), can be considered as the early stages of the chemical ordering, and the resultant nano-scale Ni-Al-rich clusters are likely to be SRO domains. Such clusters have also been referred to as clustered ordered domains in the literature.²⁷ Before the proton irradiation, the range of the proton and created vacancies were estimated utilizing a well-known ion-solid simulation code SRIM/TRIM²⁸ (see the [supplementary material](#) for further details on calculation parameters). The results of the simulations and regions selected for microstructural characterization are shown in Fig. 1. The distribution of protons as a function of depth is depicted in Fig. 1(a). This plot shows that the maximum impact lies at a depth range of ~ 10 – 12 μm . The variation in the number of vacancies generated and the displacements per atom (dpa) with target depth when irradiated with the fluence 1 (0.8×10^{18} ions/cm²) are given in Fig. 1(b). Two regions were chosen to investigate the effects of irradiation. A region at a depth of ~ 4.5 μm corresponding to 1.6×10^{-4} vacancies/Å ion and 0.15 dpa (region 1) and a region at a depth of ~ 10.5 μm corresponding to 17×10^{-4} vacancies/Å ion and 1.5 dpa (region 2) were characterized using TEM and APT. Figure 1(c) shows the variation in vacancies and dpa when irradiated under Fluence 2 (2.33×10^{18} ions/cm²). Similar microstructural changes have been observed in both cases, and therefore, as an example, a region at a depth of 2.2 mm corresponding to 1.3×10^{-4} vacancies/Å ion and 0.34 dpa (region 3) was analyzed, and the results are summarized in the [supplementary material](#), Fig. S2. A schematic showing the direction of proton irradiation with respect to sample surface and the procedure adopted for TEM and APT lift-outs is shown in Fig. 1(d). The cross-sectional area was used for all analyses.

Figure 2 shows the microstructure of region 1. The selected area diffraction pattern (SADP) recorded from a [001] FCC zone axis reveals the presence of superlattice reflections at {001} and {011} positions in addition to the FCC fundamental reflections ({002} and {022}) as opposed to only fundamental reflections in the case of the solutionized and quenched condition (refer to Fig. S1). These superlattice reflections indicate long-range ordering on the FCC lattice leading to the formation of L_{12} LRO domains or nanoprecipitates. A dark-field TEM micrograph recorded from one of the superlattice reflections in Fig. 2(b) shows the size scale and distribution of ordered L_{12} domains within the FCC matrix. The Al ion map from APT shown in Fig. 2(c)

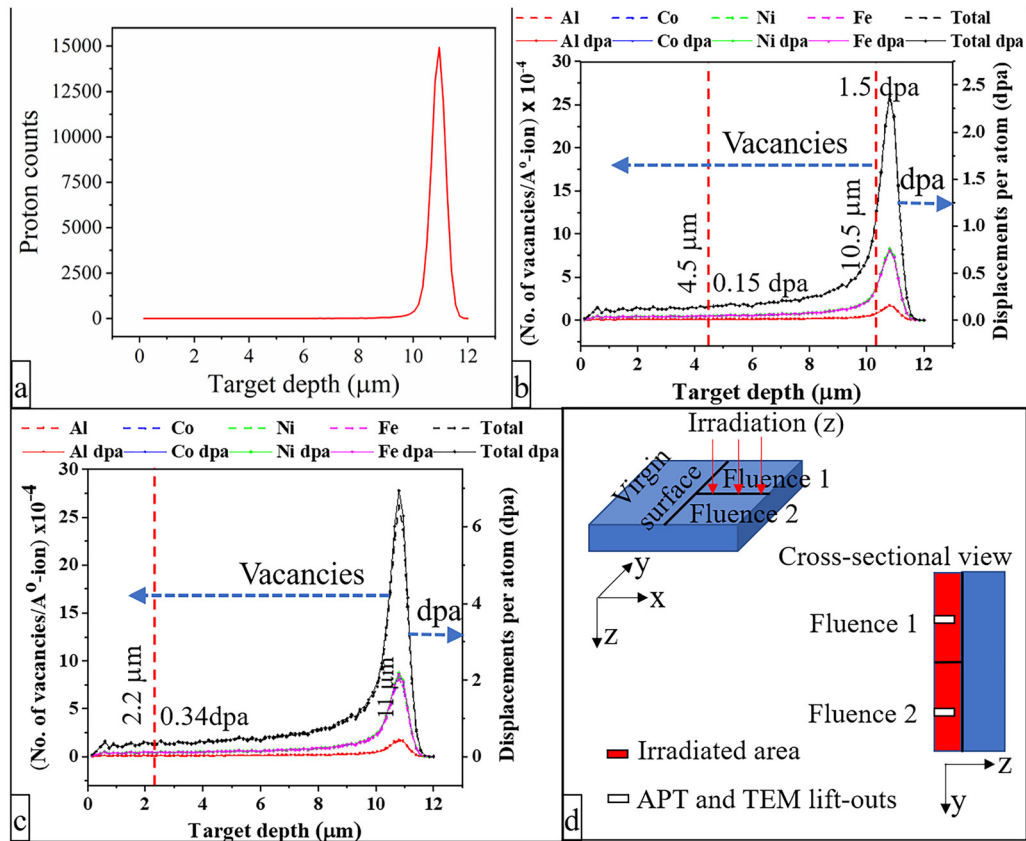


FIG. 1. (a) TRIM simulated distribution of protons as a function of target depth. (b) Number of vacancies and displacements per atom as a function of target depth when irradiated using Fluence 1. Location of the TEM and APT lift-outs is marked with red dashed lines. (c) Number of vacancies and displacements per atom as a function of target depth when irradiated using Fluence 2. Location of the TEM and APT lift-outs is marked with red dashed lines. (d) Schematic showing the direction of irradiation with respect to sample surface and the procedure adopted for making TEM and APT lift-outs. Note that the solid lines in (b) and (c) can be used as a guide to readout the number of vacancies and dpa since they overlap with each other.

reveals visible chemical partitioning between these domains and surrounding matrix as compared to the seemingly homogenous distribution in solutionized and quenched condition (refer to Fig. S1). An iso-concentration surface (or iso-surface) that separates the Al-rich and Al-lean regions, constructed using an Al concentration of 7.8 at. %, is shown in Fig. 2(d). Such an iso-surface is constructed by choosing an appropriate Al concentration that can distinguish between Al-rich and Al-lean regions through multiple surfaces/interfaces. This iso-surface shows that the Al-rich ordered domains are uniformly present throughout the microstructure. The compositional profile across this surface, as shown in Fig. 2(e), indicates that while Al-lean regions are enriched in Fe and Co, Al-rich regions are enriched in Ni as well. Comparing the structure and composition of these Ni-Al-rich domains in the quenched conditions vs the irradiated condition reveals some important differences. First, the presence of superlattice reflections in the latter signifies the transition of SRO domains into LRO domains/precipitates. Second, the Ni and Al enrichment in these domains has increased by 6 at. % and 2 at. %, respectively, after irradiation. The Ni-Al-rich domains after irradiation were found to be ~ 3 nm in size and contain ~ 37 at. % Ni and 14 at. % Al. Additionally,

Co-rich regions were also detected in the APT reconstructions. The Co ion map in Fig. 2(f) shows visible partitioning between the FCC matrix and L_{12} precipitates. However, the 40.1 at. % Co iso-surface in Fig. 2(g) shows irregular plate-shaped Co-rich regions. The concentration profile across these plate-shaped regions in Fig. 2(h) shows that the Co content of these regions is ~ 60 at. % as opposed to ~ 30 at. % in the FCC matrix. The morphology of these regions suggests defect clusters or dislocation loops.²⁹ Previously, it has been reported that a disk-shaped segregation is favorable over ring shape along dislocation loops.¹⁶ Co and Ni being slow vacancy^{17,19} but fast interstitial diffusers¹⁶ remain at the defects while Al and Fe diffuse away, leading to the observed Co-rich regions.

The TEM and APT results from region 2 are shown in Fig. 3. Similar to region 1, the SADP in Fig. 3(a) shows superlattice reflections at $\{001\}$ and $\{011\}$ positions, indicating the formation of ordered L_{12} domains/precipitates. The dark-field image recorded from one of these reflections shown in Fig. 3(b) reveals a homogenous distribution of L_{12} precipitates within the FCC matrix. APT results, shown in Figs. 3(c)–3(h), also show Ni-Al-rich domains corresponding to ordered L_{12} precipitates, and Co-rich regions, similar to region 1. Interestingly,

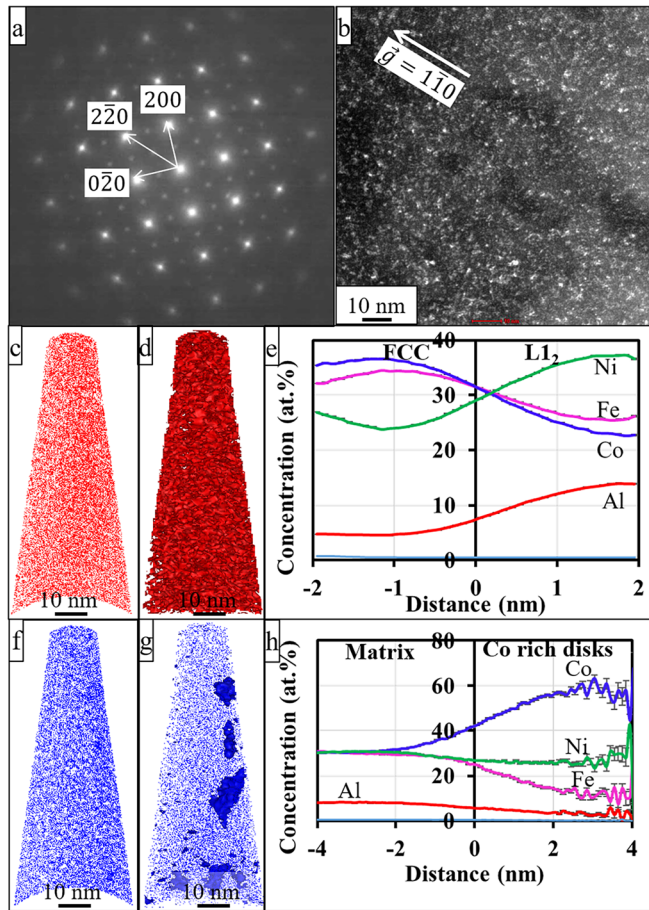


FIG. 2. Microstructural characterization of region 1. (a) Selected area diffraction pattern showing the presence of superlattice reflections along with FCC fundamental reflections indicative of ordering. (b) Dark-field micrograph recorded from one of the superlattice reflections in (a) showing the distribution of ordered L_{12} precipitates within the FCC matrix. (c) Al APT ion map shows visible partitioning. (d) Al 7.8 at. % iso-surface marking the interface between Al-rich and Al-lean regions. (e) Concentration profile showing the chemical partitioning of all elements between FCC matrix and L_{12} precipitates. (f) Co APT ion map shows visible partitioning. (g) Co 40.1 at. % iso-surfaces showing Co-rich plate/disk-shaped regions. (h) Concentration profile showing the chemical partitioning of all elements across one of the plate-shaped regions in (g).

while the size of these domains did not change significantly, the Ni-Al enrichment in region 2 is larger as compared to region 1. The Ni-Al domains in region 2 were found to contain ~ 40 at. % Ni and ~ 16 at. % Al. While the dark field micrographs in Figs. 2(b) and 3(b) show a difference in L_{12} size and distribution, it could be an artifact arising from foil thickness and diffracting condition. Iso-surface concentration profiles obtained from APT are more reliable in comparing the L_{12} size and distribution in the two cases. From Figs. 2(e) and 3(e), the L_{12} or Ni+Al enriched regions appear to be of the size ~ 2.5 and 2.7 nm in regions 1 and 2, respectively. Additionally, the number density of Co-rich plate/disk-shaped regions has significantly increased. Similar changes in the extent of ordering and composition have been observed in region 3 where the dpa lies in between regions 1 and 2.

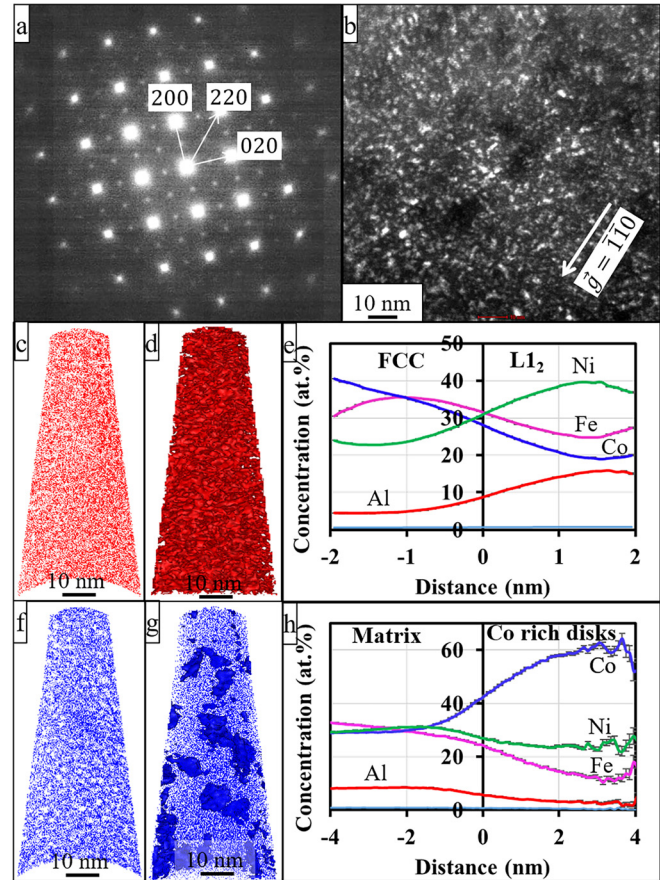


FIG. 3. Microstructural characterization of Region 2. (a) Selected area diffraction pattern showing the presence of superlattice reflections along with FCC fundamental reflections indicative of ordering. (b) Dark-field micrograph recorded from one of the superlattice reflections in (a) showing the distribution of ordered L_{12} precipitates within the FCC matrix. (c) Al APT ion map shows relatively stronger partitioning compared to region 1. (d) Al 8.3 at. % iso-surface marking the interface between Al-rich and Al-lean regions. (e) Concentration profile showing the chemical partitioning of all elements between FCC matrix and L_{12} precipitates. (f) Co APT ion map shows visible partitioning. (g) Co 40.6 at. % iso-surfaces showing Co-rich plate/disk-shaped regions. (h) Concentration profile showing the chemical partitioning of all elements across the disk-shaped regions in (g).

The microstructural characterization of region 3 is shown in the [supplementary material](#), Fig. S2.

To mimic the enhanced diffusion kinetics during irradiation, the quenched $\text{Al}_{0.3}\text{CoFeNi}$ alloy was thermally annealed at 500°C for 30 min. The thermal activation via annealing also enhances diffusion and drives the system toward equilibrium. Figure 4(a) shows the SADP from the annealed condition. Weak superlattice reflections are visible, indicating the early stages of LRO. The dark-field micrograph in Fig. 4(b) shows finer scale (relative to the irradiated samples) L_{12} precipitates. Interestingly, no visible chemical partitioning was observed in APT. However, frequency distribution analysis of Ni and Al in Fig. 4(c) reveals a nonrandom solid solution. The deviation of observed Al/Ni distribution from their respective binomial curves indicates nonrandom distribution of elements in the solid solution.

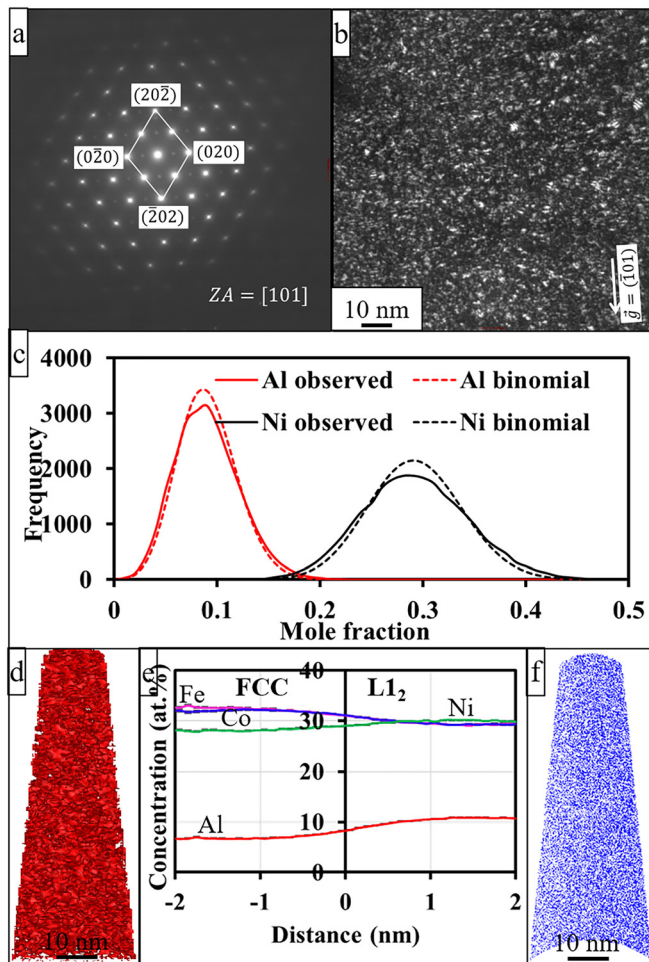


FIG. 4. Microstructural characterization of $\text{Al}_{0.3}\text{CoFeNi}$ annealed at 500°C for 30 min. (a) Selected area diffraction pattern showing the presence of superlattice reflections along with FCC fundamental reflections indicative of ordering. (b) Dark-field micrograph recorded from one of the superlattice reflections in (a) showing the distribution of ordered L_{12} precipitates within the FCC matrix. (c) Frequency distribution analysis of Al and Ni. The deviation of observed Al/Ni distribution from binomials indicates nonrandom distribution of elements in the solid solution. (d) Al 8.6 at. % iso-surface marking the interface between Al-rich and Al-lean regions. (e) Concentration profile showing the chemical partitioning of all elements between FCC matrix and L_{12} precipitates. (f) Co APT ion map showing homogenous distribution.

Additionally, constructing a concentration profile across the Al iso-surface revealed early stages of compositional partitioning. The Al 8.6 at. % iso-surface is shown in Fig. 4(d), and the corresponding concentration profile is shown in Fig. 4(e). Ni and Al enrichment to the right and Fe and Co enrichment to the left can be noted from this profile. The size of L_{12} domains as determined from the APT concentration profile is about 2 nm. In contrast to the irradiated samples, no Co-rich regions were detected in these APT reconstructions. This is evident from the Co ion map in Fig. 4(f), where a homogenous distribution of Co can be observed.

The resistance of a material to irradiation depends on how well the radiation-induced defects can be absorbed by the material. These

defects enhance diffusion kinetics and aid in driving the system toward equilibrium or get annihilated at dislocations or grain boundaries. A relatively easy path to drive phase transformations using radiation-induced defects is via chemical ordering on the parent lattice. Therefore, when the alloy consists of elements that have an inherent ordering tendency (negative enthalpy of mixing), it can be used to promote the degree of ordering, which, in turn, may improve the mechanical properties. In the current alloy, $\text{Al}_{0.3}\text{CoFeNi}$, the high negative enthalpy of mixing between Ni and Al results in a strong ordering tendency as reported earlier.²² This ordering tendency results in the formation of SRO domains even in the solutionized and quenched condition of this alloy.²² Radiation or thermally activated diffusion can transform these SRO domains into LRO domains or L_{12} precipitates. However, thermodynamics has to favor their formation, and in the current alloy, the observations can be rationalized based on the phase diagram. As reported previously,³⁰ the low temperature ($<500^\circ\text{C}$) equilibrium phases in this alloy are B2 and L_{12} . While both are ordered intermetallic compounds and have simple cubic structure, the L_{12} structure is based on isostructural ordering on the parent FCC lattice, while the B2 ordered structure is based on ordering on a BCC lattice. This structural mismatch between FCC and B2 leads to a high interfacial energy $\sim 180\text{--}660\text{ mJ/m}^2$ as compared to a very low $\sim 8\text{--}24\text{ mJ/m}^2$ interfacial energy in the case of FCC/ L_{12} interfaces.³¹ Such a high interfacial energy leads to a high thermodynamic nucleation barrier for the formation of B2 within the FCC matrix.³¹ Therefore, the metastable FCC solid solution during irradiation decomposes into a more stable FCC + L_{12} microstructure. However, it should be noted that the FCC + L_{12} microstructure is also metastable and has a higher energy as compared to the true equilibrium B2 + L_{12} microstructure.

The formation of Co-rich plate/disk-shaped regions can be rationalized based on the atomic size and diffusivity of individual elements. Apart from the chemical or electronic effects, irradiation produces two types of defects, vacancies, and interstitials,³² which often condense as loops. The vacancies enhance substitutional diffusion, and undersized elements participate in interstitial diffusion. Co and Ni being the lowest atomic size among the four elements in $\text{Al}_{0.3}\text{CoFeNi}$ HEA tend to diffuse to dislocation loops as interstitials, while Fe and Al diffuse away by vacancy diffusion. It was recently been suggested that segregation in a disk-shaped morphology is more favorable than a loop,¹⁶ which appears to be the case for $\text{Al}_{0.3}\text{CoFeNi}$.

In summary, the $\text{Al}_{0.3}\text{CoFeNi}$ HEA was chosen as a candidate alloy for combining the beneficial effects of concentrated solid solution with multiple components, and the tendency for chemical ordering. Proton irradiation of this alloy transforms the SRO domains present in the prior FCC solid solution, into LRO domains via diffusion assisted by radiation-induced defects. The resultant microstructure with ordered L_{12} domains/precipitates in a disordered FCC matrix is a widely known microstructural template for superior mechanical performance.³³ Interestingly, as reported previously,²² such L_{12} precipitation leads to an increase in the strength of the alloy without compromising the tensile ductility. While the size of the ordered domains did not change significantly, the Ni and Al enrichment in the ordered domains was found to increase with the degree of irradiation. Radiation-induced segregation of Co to defect clusters/dislocation loops was also observed, due to low vacancy diffusivity of Co, consistent with the previous studies.^{16,17} Simple thermal activation via annealing of this alloy also leads to a similar transformation of SRO

domains to LRO domains/precipitates, albeit the effect is not as pronounced. The results from this study indicate that alloys with ordering tendency can potentially show higher irradiation resistance because radiation induced defects such as vacancy cascades can lead to higher diffusion rates, thereby promoting chemical ordering within the alloy. Therefore, the resultant microstructural change, i.e., precipitation of coherent L1₂ phase, can be considered as a recovery mechanism that minimizes radiation induced damage and drives the system toward equilibrium. Simultaneously, such coherent precipitation improves the mechanical properties due to the resultant microstructure with ordered domains in a disordered matrix.

See the [supplementary material](#) for stopping range of ions in matter (SRIM) calculation information and Figs. S1 and S2.

The work was supported by the U.S. Air Force Office of Scientific Research under Grant Nos. FA9550-17-1-0395 and FA9550-20-1-0169. The authors acknowledge the Materials Research Facility (MRF) at the University of North Texas for the use of microscopy facilities.

AUTHOR DECLARATIONS

Conflict of Interest

The authors declare no conflict of interest at this time.

DATA AVAILABILITY

The data that support the findings of this study are available from the corresponding author upon reasonable request.

REFERENCES

- ¹N. Hua, W. Wang, Q. Wang, Y. Ye, S. Lin, L. Zhang, Q. Guo, J. Brechtel, and P. K. Liaw, *J. Alloys Compd.* **861**, 157997 (2021).
- ²D. B. Miracle and O. N. Senkov, *Acta Mater.* **122**, 448 (2017).
- ³Y. Shi, B. Yang, and P. K. Liaw, *Metals* **7**, 43 (2017).
- ⁴Y. Zhang, T. T. Zuo, Z. Tang, M. C. Gao, K. A. Dahmen, P. K. Liaw, and Z. P. Lu, *Prog. Mater. Sci.* **61**, 1 (2014).
- ⁵S. qin Xia, Z. Wang, T. fei Yang, and Y. Zhang, *J. Iron Steel Res. Int.* **22**, 879 (2015).
- ⁶D. S. Aidhy, C. Lu, K. Jin, H. Bei, Y. Zhang, L. Wang, and W. J. Weber, *Acta Mater.* **99**, 69 (2015).
- ⁷T. Nagase, P. D. Rack, J. H. Noh, and T. Egami, *Intermetallics* **59**, 32 (2015).
- ⁸T. Egami, M. Ojha, O. Khorgolkhuu, D. M. Nicholson, and G. M. Stocks, *JOM* **67**, 2345 (2015).
- ⁹L. R. Owen, E. J. Pickering, H. Y. Playford, H. J. Stone, M. G. Tucker, and N. G. Jones, *Acta Mater.* **122**, 11 (2017).
- ¹⁰K. Y. Tsai, M. H. Tsai, and J. W. Yeh, *Acta Mater.* **61**, 4887 (2013).
- ¹¹W. Kucza, J. Dąbrowa, G. Cieślak, K. Berent, T. Kulik, and M. Danielewski, *J. Alloys Compd.* **731**, 920 (2018).
- ¹²L. R. Owen and N. G. Jones, *J. Mater. Res.* **33**, 2954 (2018).
- ¹³F. X. Zhang, S. Zhao, K. Jin, H. Xue, G. Velisa, H. Bei, R. Huang, J. Y. P. Ko, D. C. Pagan, J. C. Neufeld, W. J. Weber, and Y. Zhang, *Phys. Rev. Lett.* **118**, 205501 (2017).
- ¹⁴C. G. Schön, M. A. Tunes, R. Arróyave, and J. Ågren, *CALPHAD: Comput. Coupling Phase Diagrams Thermochem.* **68**, 101713 (2020).
- ¹⁵Y. N. Osetsky, L. K. Béland, A. V. Barashev, and Y. Zhang, *Curr. Opin. Solid State Mater. Sci.* **22**, 65 (2018).
- ¹⁶C. Lu, T. Yang, K. Jin, N. Gao, P. Xiu, Y. Zhang, F. Gao, H. Bei, W. J. Weber, K. Sun, Y. Dong, and L. Wang, *Acta Mater.* **127**, 98 (2017).
- ¹⁷C. M. Barr, J. E. Nathaniel, K. A. Unocic, J. Liu, Y. Zhang, Y. Wang, and M. L. Taheri, *Scr. Mater.* **156**, 80 (2018).
- ¹⁸K. Jin, C. Lu, L. M. Wang, J. Qu, W. J. Weber, Y. Zhang, and H. Bei, *Scr. Mater.* **119**, 65 (2016).
- ¹⁹W. Y. Chen, J. D. Poplawsky, Y. Chen, W. Guo, and J. W. Yeh, *Materialia* **14**, 100951 (2020).
- ²⁰S. Q. Xia, X. Yang, T. F. Yang, S. Liu, and Y. Zhang, *JOM* **67**, 2340 (2015).
- ²¹B. Kombaiah, K. Jin, H. Bei, P. D. Edmondson, and Y. Zhang, *Mater. Des.* **160**, 1208 (2018).
- ²²S. Dasari, A. Jagetia, A. Sharma, M. S. K. K. Y. Nartu, V. Soni, B. Gwalani, S. Gorsse, and R. Banerjee, *Acta Mater.* **212**, 116938 (2021).
- ²³G. S. Was, T. R. Allen, J. T. Busby, J. Gan, D. Damcott, D. Carter, M. Atzmon, and E. A. Kenik, *J. Nucl. Mater.* **270**, 96 (1999).
- ²⁴L. Dai, G. Niu, and M. Ma, *Materials* **13**, 2910 (2020).
- ²⁵P. Wang and G. S. Was, in *Proceedings of the 18th International Conference on Environmental Degradation of Materials in Nuclear Power Systems—Water Reactors, Minerals, Metals, & Materials Series* (Springer, 2019), pp. 1461–1474.
- ²⁶J. M. Young, S. Singh, T. A. Byers, D. C. Jones, and B. Rout, *Nucl. Instrum. Methods Phys. Res., Sect. B* **443**, 79 (2019).
- ²⁷R. Zhang, S. Zhao, J. Ding, Y. Chong, T. Jia, C. Ophus, M. Asta, R. O. Ritchie, and A. M. Minor, *Nature* **581**, 283 (2020).
- ²⁸J. F. Ziegler, M. D. Ziegler, and J. P. Biersack, *Nucl. Instrum. Methods Phys. Res., Sect. B* **268**, 1818 (2010).
- ²⁹T. Yang, S. Xia, W. Guo, R. Hu, J. D. Poplawsky, G. Sha, Y. Fang, Z. Yan, C. Wang, C. Li, Y. Zhang, S. J. Zinkle, and Y. Wang, *Scr. Mater.* **144**, 31 (2018).
- ³⁰S. Dasari, B. Gwalani, A. Jagetia, V. Soni, S. Gorsse, and R. Banerjee, *Sci. Rep.* **10**, 4836 (2020).
- ³¹B. Gwalani, S. Gorsse, D. Choudhuri, M. Styles, Y. Zheng, R. S. Mishra, and R. Banerjee, *Acta Mater.* **153**, 169 (2018).
- ³²J. W. Glen, *Adv. Phys.* **4**, 381 (1955).
- ³³R. C. Reed, *The Superalloys Fundamentals and Applications* (Cambridge University Press, 2006).